Aeroelastic behavior of a flag in ground effect

Daniele Dessi[a,*], Saverio Mazzocconi[b]

[a]*INSEAN-CNR*
National Research Council
Via di Vallerano 139, 00128 Rome - Italy
[b]*INSEAN-CNR*
National Research Council
Via di Vallerano 139, 00128 Rome - Italy

Abstract

The aeroelastic behavior of a flexible plate subjected to a uniform axial flow is investigated in the presence of ground effect due to a rigid plane placed parallel to the initial plate position. The ground effect reduces the flutter inflow velocity as it occurs for wings and strengthens the possibility of using the flag for extracting energy from winds and currents. The numerical analysis is carried out assuming that both the unsteady potential incompressible flow and the plate can be described with 2D models, a lumped vortex panel method and a nonlinear Euler-Bernouilli beam model, respectively, without losing the essential features of the fluid-structure interaction. Asymmetry of post-critical behavior (limit-cycle oscillations) and sensitivity of the results with respect to the main flag parameters (distance from the ground, mass ratio and damping) have been also considered, including also energy splitting over the identified proper orthogonal modes. The investigated reduction of the flutter velocity in ground effect has been also confirmed with preliminary experimental tests relative to a polypropilene flag with and without a rigid panel placed at one-chord distance.

Keywords: aeroelasticity, flutter, ground effect, energy harvesting

*Corresponding author: daniele.dessi@cnr.it, tel. +39 0650299254, fax. +39 065070619

1. Introduction

The flutter of a plate clamped at the leading edge (LE) and subjected to a uniform axial flow is an amazing and challenging problem from several points of view. First of all, it is a thorough example of fluid-structure interaction, and in particular of aeroelastic instability. It is relatively more complex than flutter of wings (Theodorsen (1935)) or panel flutter (Dowell (1966)) but rather easy to test in a wind tunnel (see Watanabe et al. (2002a)). This problem was not tackled as it has been done recently until some applications were focused like oronasal snoring (Huang (1995)), paper flutter of printing machines (Watanabe et al. (2002a)), energy harvesting devices (Tang et al. (2009), Doar and Michelin (2011)) and further applications may be hopefully found as mathematical modelling of some instability phenomena in nature takes place (see, for instance, some cases of the wind-plants interaction discussed by De Langre (2012)). A second reason for addressing this problem is its intrinsic nonlinear nature. Due to its high flexibility, the structure experiences large amplitude oscillations which increase the bending stiffness of the plate and determine the nonlinear dependence of the restoring force on the displacement. Due to the relevant variation of boundary conditions, aerodynamic forces can not be linearized as well. The overall behavior of the coupled system, parametrically dependent on the flow velocity, exhibits a transition from the zero equilibrium solution (stable fixed point) to stable periodic oscillations (limit cycle) following different bifurcation scenarios (Tang and Paidoussis (2007), Alben and Shelley (2008), Eloy et al. (2012)). The system dynamics generally shows a pitchfork type Hopf bifurcation also if in some cases knee-like bifurcations may occur (see, in particular, Eloy et al. (2012)). A third reason that pushes researchers toward this problem is connected to the possibility of using the fluttering plate for extracting energy from the flow, *i.e.*, as an energy harvesting device (Doar and Michelin (2011), Tang et al. (2009)).

Next, the term *plate* will be preferred to underline the structural aspects, and the term *flag* will be preferably used instead if aerodynamical or aeroelastic issues are pertinent. The reader is also referred to Tang and Paidoussis (2007) for a clarification about the different names used for denoting this flexible and waving structure, *i.e.*, plate, flag, sheet or strip.

One of the key points for using the flag as an energy harvesting device is the onset of self-sustained oscillations. For a given flag, it depends on the inflow speed V which has to be larger than the critical velocity, also named linear flutter speed V_{LF}. If the bifurcation is subcritical up to small amplitudes and turns to be supercritical for larger ones (knee-like bifurcations), the stable limit cycle (LC)

may start at a velocity lower than the linear flutter velocity. The velocity at which this phenomenon occurs is called nonlinear flutter velocity V_{NF}. This may imply that, for an inflow velocity such that $V_{NF} < V < V_{LF}$, a sudden and temporary change of velocity direction (like a vertical gust see Dessi and Mastroddi (2008)) can be sufficient for exciting the LC oscillations (LCOs). The effect of flexibility of the flag support has also a positive effect on diminishing the linear flutter speed as shown by Tang et al. (2009). In fact, the authors showed that the flutter velocity decreases with the spring stiffness modelling the flexibility of the strut.

In this paper we intend to explore another mechanism for reducing the flutter speed, which is provided by the presence of a rigid flat plate placed close and parallel to the flag at rest. This rigid plate may represent a wall if the flag is placed in vertical position or the ground if the flag plane is horizontal (in the latter case, there is an immediate similarity with the problem of wings flying close to the ground). There have been several numerical evidences in the case of 2D and 3D lifting surfaces (*e.g.*, see Nuhait and Mook (2010) and Dessi et al. (2012)) that the so-called ground effect (GE) makes the flutter speed to reduce. The GE is different with respect to the confinement effect provided by a channel flow and discussed by Doar et al. (2011). In the latter, the rigid panels are still aligned with the inflow velocity but orthogonal to the flag plane. The decrease of the flutter velocity is due to the fact that the channel makes the flow mainly two-dimensional, and numerical simulations shows that 2D analysis predicts flutter at lower speeds with respect to considering the problem in 3D.

The investigation of flags in GE is herein carried out with numerical simulations adapting to the present case the approach developed by Tang and Paidoussis (2007) for the 2D analysis of elastic plates subjected to axial inviscid and incompressible flow in an unbounded domain. The unsteady lumped vortex method (Katz and Plotkin (2001)) is then used for the calculation of the aerodynamic force acting on the flag contour along with the method of images for imposing the impermeability condition on the straight line representing the ground. From the structural point of view, the Euler-Bernouilli beam model with geometrical nonlinearities due to curvature and with a Kelvin-Voigt damping model is considered appropriate for describing the 2D motion of a plate section. To evaluate the GE on the flag dynamics, a sensitivity analysis of the dependence of the critical velocity V_{LF} and of the LCO amplitudes with respect to the ground distance h_g is carried out. The nonlinear analysis focuses on the LCOs of the generalized coordinates and of the TE point as a representative point on the physical flag. Asymmetry of bifurcations due to breaking of aerodynamic symmetry by the ground is presented and discussed. Proper orthogonal decomposition (POD) is also applied to the flag

self-excited oscillations and the energy of the identified modes is related to the inflow velocity and to the distance from the ground. Some experimental tests concerning the flutter behavior of the flag were also carried out and preliminary results confirming the decrease of flutter speed in GE will be presented. These tests used the towing tank carriage running over a long water basin ($500\ m$) for carrying on the experimental setup (flag plus support) so as to be subjected to the apparent wind velocity. Coming back to the modelling of the flag behavior, two cases have been considered because of the sensitivity of the flag dynamics to the damping and the mass ratio: the first one has a mass ratio equal to that of the tested physical flag and the second one, already considered by Tang and Paidoussis (2007) in infinite domain, allows highlighting to a greater extent some nonlinear characteristics.

2. Modelling and numerical methodology

2.1. Equation of motion of the plate

In Fig. 1 the main geometrical and kinematic parameters of the rectangular flag are defined. The length of the plate in the downstream direction is denoted with c (also indicated as the flag chord in the following), b is the transversal length (or the flag span), δ denotes the plate thickness. The reference system is set so as the plate at rest lies in the plane $(\bar{x}, \bar{y})$ and the undisturbed velocity direction is parallel to the unit vector $\vec{e}_1$. Focusing on the plate section obtained with the plane $\bar{y} = \text{const}$, the components of the displacement $\vec{u}$ in the $\vec{e}_1$ and $\vec{e}_3$ directions are $\bar{u}(\bar{s}, t)$ and $\bar{w}(\bar{s}, t)$, respectively, with $\bar{s}$ and t the curvilinear abscissa and the time. In the perspective of exploiting large amplitude oscillations for energy harvesting, the plate has to be very thin, *i.e.*, $\delta \ll c$. The condition $b/c \gg 1$ which is required for describing the plate motion with a beam model (geometrically, a longitudinal section along the $\bar{x}$ direction) is not matched in the present application. Nonetheless, in axial flow conditions, the plate mainly bend around the $\bar{y}$-axis. Thus, with $b/c = O(1)$, the induced loads allow using a 2D description for both the fluid and the structure with a satisfactory accuracy. The structure is then modelled as an Euler-Bernouilli beam ($\delta \ll c$) with nonlinear terms accounting for the increase of the stiffness under large deformations. The type of boundary conditions ($\vec{u} = 0$ at the LE) determines that the strain ε on the mean plate surface is negligible and inextensibility of the plate can be assumed. The structural model adopted in this investigation is the same used by Tang and Paidoussis (2007) for the flag and previously introduced for a similar problem (pipes conveying fluid) by Semler et al. (1994).

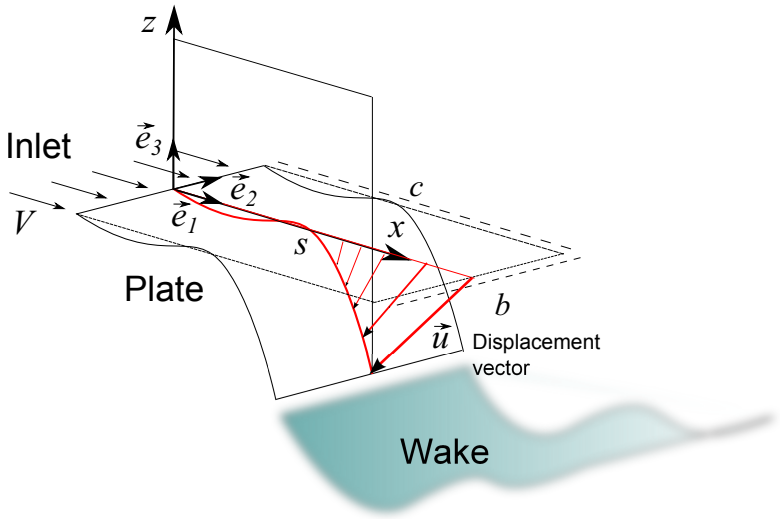

Figure 1: Main geometrical parameters and kinematic variables

Under the hypotheses previously stated, the equations of motion of an Euler-Bernouilli beam subjected to large displacements can be obtained by using the Hamilton principle and a Lagrangian function with a Lagrange multiplier for imposing the inextensibility condition on the mean plane. Thus, the Lagrange function for unit span length ℓ is:

$$\ell = \frac{1}{2}\left\{m\left(\bar{u}_t^2 + \bar{w}_t^2\right) - \left(EA\,\varepsilon^2 + D\,\kappa^2\right) + \lambda\left[1 - \left(1 + \bar{u}_{\bar{s}}\right)^2 - \bar{w}_{\bar{s}}^2\right]\right\}, \qquad (1)$$

where m the mass per unit length, E is the Young modulus, A the area of the beam transversal section, D the bending stiffness, ε the strain, κ the curvature and λ the Lagrange multiplier. The subscripts indicate derivation with respect to the written variable. The advantage of this formulation lies in the fact that more complex material can be described just by adding new terms. It is worth recalling that both the strain ε and the curvature κ for large displacements have a dependency on both the displacement components $\bar{u}$ and $\bar{w}$:

$$\varepsilon = \sqrt{\left(1 + \bar{u}_{\bar{s}}^2\right) + \bar{w}_{\bar{s}}^2} - 1, \qquad \kappa = \frac{\bar{w}_{\bar{s}\bar{s}}\left(1 + \bar{u}_{\bar{s}}\right) - \bar{w}_{\bar{s}}\bar{u}_{\bar{s}\bar{s}}}{\left(1 + \bar{u}_{\bar{s}}\right)^2 + \bar{w}_{\bar{s}}^2}. \qquad (2)$$

The above relations, once substituted in Eq. 1, makes the computation of the derivatives appearing in the Lagrange equations cumbersome. Therefore, it is

convenient that the expressions for both curvature and strain are expanded in series. In performing this approximation, the critical point is to retain terms up to the same order uniformly.

Moreover, thank to the inextensibility condition, the horizontal displacement $\bar{u}(\bar{x},t)$ can be eliminated from the equations. Next, the following non-dimensional quantities are defined:

$$x=\frac{\bar{x}}{c},\quad z=\frac{\bar{z}}{c},\quad u=\frac{\bar{u}}{c},\quad w=\frac{\bar{w}}{c},\quad s=\frac{\bar{s}}{c},\quad h=\frac{h_g}{c},\quad \tau=\frac{t}{\sqrt{\rho_S\delta c^4/D}} \tag{3}$$

$$f^*=\bar{f}\sqrt{\rho_S\delta c^4/D},\quad \alpha=\frac{a}{\sqrt{\rho_S\delta c^4/D}},\quad f_L=\frac{F_L}{\rho_f V^2},\quad f_D=\frac{F_D}{\rho_f V^2}, \tag{4}$$

where, in Eq. 4, the symbols denoting the structural frequency and damping, the lift and the drag force, respectively, appear in non-dimensional and dimensional form. Thus, the final equation in the vertical displacement w alone is, in non-dimensional form,

$$\begin{aligned}&\ddot{w}+(1+\alpha\frac{\partial}{\partial\tau})\left[w''''\left(1+w'^2\right)+4w'w''w'''+w'''^2\right]\\&+w'\int_0^s(\dot{w}'^2+w'\ddot{w}')ds-w''\int_s^1\left[\int_0^s(\dot{w}'^2+w'\ddot{w}')ds\right]ds\\&=\mu U_R^2(f_L-w'f_D+w''\int_s^1 f_D\,ds)\,.\end{aligned} \tag{5}$$

$$v(s)=-\frac{1}{2}\int_0^s w'^2(\eta)\,d\eta \tag{6}$$

The form of Eq. 5 allows solving this equation with Galerkin projection over the first M dry vibration modes of a clamped-free plate. Thus, assuming:

$$w(x,t)=\sum_{h=1}^{M}q_h(t)\psi_h(x) \tag{7}$$

the form of the 'modal' equations is:

$$\begin{aligned}&\ddot{q}_h+A_h\,q_h+aA_h\dot{q}_h+B_{hmnl}\,q_mq_nq_l+aB_{hmnl}\,(\dot{q}_mq_nq_l+q_m\dot{q}_nq_l+q_mq_n\dot{q}_l)\\&+C_{hmnl}q_m\,(\dot{q}_n\dot{q}_l+q_n\ddot{q}_l)=f_h,\end{aligned} \tag{8}$$

with A_h the linear part, B_{hmnl} and C_{hmnl} 3-rd order tensors providing the coefficients of cubic terms. In particular, comparing Eq. 8 with Eq. 5, the coefficients

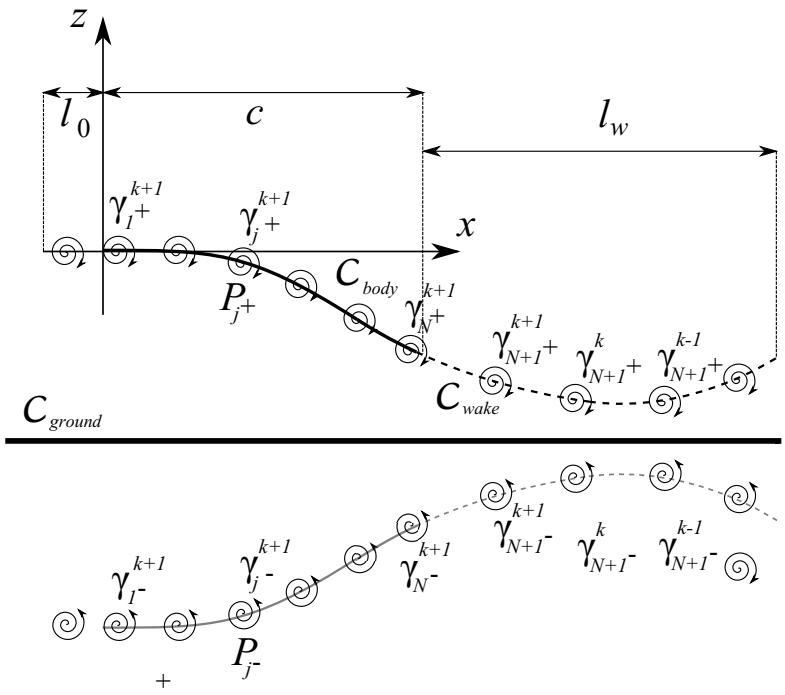

Figure 2: Distribution of lumped vortices along the body contour and the wake.

A_h and B_{hmnl} are the linear and nonlinear part of the stiffness, respectively, the coefficients aA_h and aB_{hmnl} represent the linear and nonlinear part of the damping, respectively, because damping proportional to stiffness has been chosen. It is worth noting that the term $C_{hmnl}q_m\left(\dot{q}_n\dot{q}_l + q_n\ddot{q}_l\right)$ is due to the elimination of the variable u since structural mass is not initially time depending (added mass effect are accounted for in the expression of aerodynamic forces).

2.2. Model of the fluid flow

This section addresses the mathematical description of the aerodynamic loads on an oscillatory flag section in GE as a first step for defining its comprehensive aeroelastic model (see Fig. 2). The flow is assumed to be incompressible, inviscid, and initially irrotational. Therefore, the formulation is based on potential flow theory. As stated before, for sake of simplicity, the flow is also assumed to be two-dimensional without compromising the essential features characterizing the fluid-structure interaction. Under these hypotheses, the conservation of the flow mass becomes,

$$\nabla^2\varphi = 0, \tag{9}$$

where $\varphi(\vec{x},t)$ is the flow potential perturbation, and $\vec{x} = \{x,z\}^T$ the vector of space coordinates. The impermeability on the flag contour $\mathcal{C}_{body}$ and on the ground straight line $\mathcal{C}_{ground}$ (see Fig. 2), yields:

$$\frac{\partial\varphi}{\partial n} = \vec{v}_F \cdot \vec{n} = \vec{v}_B \cdot \vec{n}, \quad \vec{x} \in \mathcal{C}_{body} \quad \text{and} \quad \frac{\partial\varphi}{\partial n} = \vec{v}_F \cdot \vec{n} = 0, \quad \vec{x} \in \mathcal{C}_{ground}, \tag{10}$$

where $\vec{v}_F$ is the flow velocity, $\vec{v}_B$ is the body vector velocity and $\vec{n}$ the local outward normal vector to the body. Since the flow is considered unperturbed at large distances $\vec{r}$ from the body, the perturbation potential φ is imposed to be zero at infinity, *i.e.*,

$$\varphi \to 0 \qquad \text{as} \quad \vec{r} \to \infty. \tag{11}$$

The wake shed by the trailing edge of the airfoil is considered as a contact discontinuity from an aerodynamical point of view. Geometrically, its configuration depends on the point where the vortex is released by the trailing edge and convected downstream with the free stream velocity. Recalling the linearized Bernoulli theorem, the condition upon the wake $\mathcal{C}_{wake}$ reduces to

$$\frac{D_w \Delta\varphi}{Dt} = 0 \qquad \vec{x} \in \mathcal{C}_{wake}, \tag{12}$$

where $D_w(\cdot)/Dt$ accounts for the total derivative along the wake $\mathcal{C}_{wake}$ with the convective velocity $\vec{v}_c$ which is the average between the upper and lower velocity at the contact discontinuity. Assuming that $\vec{v}_c$ is zero, Eq. (12) states that in an air frame of reference the quantity $\Delta\varphi$ does not change in time and keeps constant whenever shed by the flag trailing edge.

Equation 10 can be specialized furthermore. The flow velocity $\vec{v}_F$ is the sum combination of the self-induced velocity and the free-stream velocity $\vec{v}_\infty$:

$$\vec{v}_F = \vec{v}_\infty + \vec{v}_b + \vec{v}_w, \tag{13}$$

where $\vec{v}_b$ and $\vec{v}_w$ represent the contribution of the body and the wake, respectively, to the self-induced velocity. Substituting Eq. 13 into the expression of the body boundary conditions (Eq. 10) yields:

$$(\vec{v}_\infty + \vec{v}_b + \vec{v}_w) \cdot \vec{n} = \vec{v}_B \cdot \vec{n}. \tag{14}$$

To calculate the aerodynamic forces on the flag, the 2D lumped vortex panel method (LVPM, see Katz and Plotkin (2001)) has been implemented. The 2D

flag contour (see Fig. 2) is divided into N_a rectilinear elements (panels) including those placed on the rigid inlet. Additional elements are considered on the wake but the number of these elements (N_w) is variable depending on the wake evolution after simulation have started. With respect to this discretization, let us indicate with i the collocation point on the body and with j the lumped vortex. For each panel. the discrete vortex is placed at $1/4$ of the panel chord, whereas the collocation point is assumed to be at $3/4$ of the panel chord. From Eq. 14, the body self-induced velocity relative to the element i can be expressed as:

$$\vec{v}_b^{(i)} = \vec{v}_\infty^{(i)} + \vec{v}_w^{(i)} - \vec{v}_B^{(i)} \tag{15}$$

When considering ground-effect, it is necessary to distinguish between the flow perturbation in the collocation point i due to the body vorticity and to its image. Thus,

$$\vec{v}_b^{(i)} = \vec{v}_{b^+}^{(i)} + \vec{v}_{b^-}^{(i)} \tag{16}$$

with $\vec{v}_{b^+}^{(i)}$ and $\vec{v}_{b^-}^{(i)}$ the velocity perturbation due to the body and to the image vorticity, respectively. Next, the influence of the single j vortex on the normal velocity at each collocation point will be accounted for. Taking the velocity component normal to the body contour and assuming a unit-strength vortex for both the body and its image, it follows:

$$\vec{v}_{b,j}^{(i)} \cdot \vec{n}^{(i)} = \vec{v}_{j^+}^{(i)} \cdot \vec{n}^{(i)} + \vec{v}_{j^-}^{(i)} \cdot \vec{n}^{(i)} = A_{ij}^+ + A_{ij}^- \tag{17}$$

with $\vec{n}^{(i)} \equiv (\sin\alpha^{(i)}, \cos\alpha^{(i)})$ and $\alpha^{(i)}$ the local element slope. Since $\gamma_j = \gamma_{j^+} = -\gamma_{j^-}$, considering the contribution of all the vortices:

$$\sum_{j=1}^{N_b} A_{ij}^+ \gamma_j - \sum_{j=1}^{N_b} A_{ij}^- \gamma_j = \sum_{j=1}^{N_b} A_{ij} \gamma_j = \vec{v}_b^{(i)} \cdot \vec{n}^{(i)}, \tag{18}$$

with $A_{ij} = A_{ij}^+ + A_{ij}^-$. The normal velocity component due to the motion of the flag ($\vec{v}_B^{(i)} \equiv (\dot{u}^{(i)}/U_R, \dot{w}^{(i)}/U_R)$) as well as the free-stream contribution ($\vec{v}_\infty^{(i)} \equiv (1, 0)$) are known from kinematic equations and will be transferred to the right-hand side of the equation. The correspondence between vortex elements and structural mesh will be addressed later.

The velocity induced by the last vortex shed by TE, $\gamma_{w,1}$, is unknown as well. Because of Kelvin condition, $\gamma_{w,1}$ accounts for the variation of circulation between

two successive time steps, say $k+1$ and k, which need to be explicitly defined. Thus,

$$\sum_{j=1}^{N_a} \gamma_j^{k+1} + \gamma_{w,1}^{k+1} = \Gamma^k = \sum_{j=1}^{N_a} \gamma_j^k, \tag{19}$$

with $\gamma_{w,1}^{k+1}$ the unknown intensity of the last released vortex and Γ^k the overall circulation around the lifting body. Setting $\gamma_{N+1}^{k+1} = \gamma_{w,1}^{k+1}$, the previous equation is simply recast as:

$$\sum_{j=1}^{N_a+1} \gamma_j^{k+1} = \Gamma^k. \tag{20}$$

Similarly, in Eq. 18, the unknown vortex strength has to be moved to the l.h.s.. The strength of the other wake vortices is known from the previous time steps and their effect on the normal velocity remains on the r.h.s.. In particular:

$$\vec{v}_w^{(i)} = \vec{v}_{w^+}^{(i)} + \vec{v}_{w^-}^{(i)} \tag{21}$$

with

$$\vec{v}_{w^+}^{(i)} \equiv (v_{1,w^+}^{(i)},\, v_{3,w^+}^{(i)}) = \frac{1}{2\pi} \sum_{j=1}^{N_w} \frac{\gamma_j}{(z_i - z_j)^2 + (x_i - x_j)^2} \left\{ \begin{array}{c} z_i - z_j \\ x_j - x_i \end{array} \right\}, \tag{22}$$

$$\vec{v}_{w^-}^{(i)} \equiv (v_{1,w^-}^{(i)},\, v_{3,w^-}^{(i)}) = -\frac{1}{2\pi} \sum_{j=1}^{N_w} \frac{\gamma_j}{(z_i + z_j + 2h)^2 + (x_i - x_j)^2} \left\{ \begin{array}{c} z_i + z_j + 2h \\ x_j - x_i \end{array} \right\}, \tag{23}$$

where $\vec{v}_{1,w^\pm}^{(i)}$ and $\vec{v}_{3,w^\pm}^{(i)}$ denote the components of the velocity induced by the wake and its image at the collocation point i, respectively (note that on the r.h.s. the vector components are enclosed between brackets). Finally, the system of linear equations to be solved is:

$$\sum_{j=1}^{N_a} A_{ij}^{k+1}\, {\gamma_j}^{k+1} + A_{i\,N_a+1}^{k+1} \gamma_{N_a+1}^{k+1} = \vec{v}_b^{(i)} \cdot \vec{n}^{(i)} \tag{24}$$

$$\sum_{j=1}^{N_a+1} \gamma_j^{k+1} = \Gamma^k. \tag{25}$$

The unsteady pressure field $\Delta p(x,t)$ over the i-th panel can be obtained after the vortex intensities have been determined with Eq. 24:

$$\Delta p^{(i)} = \left[\left(-\frac{\dot{u}^{(i)}}{U_R} + 1 + v_{1,w}^{(i)} \right) \cos\alpha^{(i)} + \left(\frac{\dot{w}^{(i)}}{U_R} - v_{3,w}^{(i)} \right) \sin\alpha^{(i)} \right] \frac{\gamma_i}{\Delta s_i}$$

$$+\frac{1}{U_R}\frac{\partial}{\partial\tau}\left(\sum_{j=1}^{i}\gamma_j\right), \tag{26}$$

where the dependence on the time step k has been omitted for sake of simplicity.

2.3. Coupled system

The pressure field along the flag provides the lift force ($f_L = \Delta p\,\vec{n}\cdot\vec{e}_3$) and the drag force ($f_D = \Delta p\,\vec{n}\cdot\vec{e}_1 + C_D$) in Eq. 5. Considering the discretized form of the lift and drag forces, *i.e.*,

$$f_L^{(i)}(t) = \Delta p^{(i)}(t)(\vec{n}^{(i)}\cdot\vec{e}_3), \qquad f_D^{(i)}(t) = \Delta p^{(i)}(t)(\vec{n}^{(i)}\cdot\vec{e}_1) + C_D^{(i)} \tag{27}$$

and projecting on h-th mode shape $\psi_h = \{\psi_h^{(1)}, \psi_h^{(2)}, \ldots\}^T$ allows computing the modal force f_h on the r.h.s. of Eq. 8. We have implicitly assumed so far that there is a perfect correspondence between the number of points N_s used for describing the structure (plate section), *i.e.*, the 2D beam geometry, and the aerodynamic discretization with N_a vortex elements on the flag. Because of the modal approach, there is no limitation in using more points in evaluating the mode shapes while the number of panels have an impact on the computational cost of the aerodynamic load as well as the number of wake panels. Assuming $N_s = \nu\, N_a$ with ν an integer (in the present calculations $\nu = 5$), implies that there are $\nu + 1$ structural points for each panel. As the indexes labelling Δp and $\vec{n}$ in Eq. 27 vary over different ranges, a uniform Δp is assumed over along the structural elements belonging to the same panel (the lift and the drag force on each panel element will differ because of different normal vectors). On the other hand, the computation at $3/4$-chord body velocity in each panel (see $\vec{v}_B$ in Eq. 15) requires a linear interpolation on the structural velocity data.

The Houbolt scheme has been adopted as time-marching method for integrating Eq. 8 because, as already pointed out by Tang and Paidoussis (2007), is stable, accurate and efficient also in presence of nonlinear inertial terms. Coefficients of the time-marching method are those reported in Tang and Paidoussis (2007) and, for avoiding numerical instabilities due to large added mass, the technique introduced by Belanger et al. (1995) has been implemented. Comparisons with 4-th order Runge-Kutta scheme shows that in the present case simulation time is halved using the Houbolt routine.

3. Experimental set-up

Preliminary tests for verifying experimentally the beneficial GE in reducing the flutter speed have been carried out at the CNR-INSEAN towing-tank basin.

Figure 3: Experimental set-up: test section on the towing-tank carriage.

The experimental approach for the tests consists in exploiting the towing-tank motion for generating an inflow velocity equal and opposite to the carriage speed. The test section for the flag is placed on-board the towing-tank carriage usually devoted to tow the ship scaled models. The towing-tank carriage can reach speeds up to $15\ m/s$ but safe runs at high speeds covers no more than $2/3$ of the $450\ m$ basin length. The test section, placed on the forward part of the carriage for minimizing blockage effects due to the carriage super-structure, is schematically shown in Fig. 3. The flag is placed with the LE side parallel to the vertical direction so as to avoid any initial deflection of the polypropylene flag because of gravity. The LE of the flag is then attached to a thin metallic plate which provides the aerodynamic inlet and plate clamping on one side. This thin plate is connected downward to a thicker plate and then to a beam to provide a rigid connection not interfering with aerodynamics. Wires are also used for limiting vibrations of the support.

The presence of the ground is mimicked by adding a rigid screen parallel to the flag plane at rest. The flag motion is supposed to remain 2D sa as the edge of the flag is representative of the whole plate motion. A screen is placed parallel to the undeformed flag plane for simulating the presence of the ground. Two high-speed cameras (DALSA-FALCON with a 1.4 Megapixel CMOS, 1024 x 1280 image resolution) dedicated to image acquisition were mounted above the flag for recording the swaying of the upper plate edge. The acquisition frequency was set to $200\ Hz$ and the acquired images have a spatial resolution of about $0.36\ mm/px$. It is worth underlying again that the experimental effort was devoted to verify

through the analysis of the flag motion the effectiveness of the ground plate in inducing flutter at velocities lower than those recorded without it.

4. System dynamics

4.1. Numerical parameters and initial conditions

The numerical results shown in the following will focus on the aeroelastic behavior of the flag in ground effect. The behavior of the flag without the ground (infinite domain) will be also considered for comparison. The latter can be also treated as a particular case of the ground effect problem setting h sufficiently large with negligible differences.

The characteristics of the plate for the numerical simulations have been chosen to be similar to those relative to the polypropylene flag actually tested for obtaining an experimental evidence of the flutter speed reduction in GE. The main dimensions are $c = 0.317\,m$, $b = 0.200$ and $\delta = 0.0005$ with a rigid inlet length l_0 equal to $0.044\,m$. The flag has a Young modulus $E = 1.4GPa$ and a density ρ_S of $910\,kg/m^3$ thus determining a mass ratio $\mu = 0.76$. Reasonable values for the the damping ratio and the drag coefficient have been set to $\alpha = 0.025$ and $C_D = 0.001$. Due to the relevance of mass ratio μ and damping coefficient α in determining the flutter characteristics of the flag, the plate configuration already analyzed by Tang and Paidoussis (2007) ($h = \infty$, $\mu = 0.2$ and $\alpha = 0.001$) is also reconsidered here in GE.

The initial condition was given by imposing at $t = 0$ a deformation according to the first bending mode, with no imposed velocity. The stationary solution (either a fixed point or a stable LCO depending on the inflow velocity) can be reached regardless the value of the first mode amplitude, as the preliminary investigation of the basin of attraction has shown. To speed up calculations, an initial condition close to the LC was preferred beyond the critical flutter speed with $q_1(0) = 1 \cdot 10^{-2}$ and $q_i(0) = 0$ for $i > 1$. For $U < U_{LF}$, the value of $q_1(0)$ was set to $q_1(0) = 1 \cdot 10^{-5}$ for putting in evidence the instability of the fixed point solution.

4.2. Onset of flutter and post-critical vibrations in GE for $\mu = 0.76$

One of the main achievement of the present investigation is the analysis of the dependence of the critical inflow velocity speed U_F on the (nondimensional) ground clearance h shown by Fig. 4. It is evident that, as long as h decreases, the non-dimensional flutter velocity, $U_{LF}(h)$, reduces, whereas for $h \to \infty$, it reaches

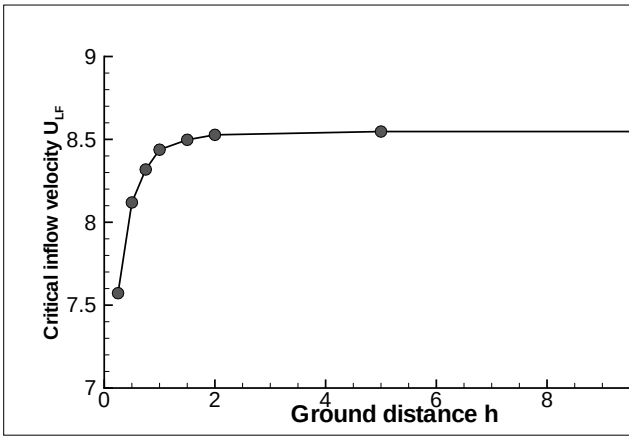

Figure 4: Dependence of the flutter speed with respect to the distance from the ground ($\mu = 0.76$ and $\alpha = 0.025$).

the value calculated with no GE. The non-dimensional flutter speed in infinite domain is $U_{LF}(\infty) = 8.59$ for the geometry and material properties considered here. At $h = 1$, the reduction is about 1.3%, and at $h = 0.25$ the flutter speed is 11.4% lower than the critical speed at $h = \infty$. This result confirms the prediction made by Dessi et al. (2012) about the the similar reduction of flutter speed experienced by a plunging and pitching 2D wing profile in GE.

For $U > U_{LF}$, stable LCOs appear as a consequence of the balancing between destabilizing aerodynamical and stabilizing structural forces. In fact, large amplitude deformations increase the flag stiffness and then the structural restoring force. The snapshots of the flag motion at several time instants are depicted in Figs. 5 and 6 for $h = 0.5$. The amplitude of the motion (and so the mechanical energy extracted from the flow) clearly grows as U is increased from a near-critical velocity (Fig. 5) to a post-critical regime (Fig. 6). It is evident also that the tip is forced to move upstream due to the inextensibility condition and that the flag deflection is not symmetric with respect to its undisturbed position. If the infinite domain case is considered, the flag motion looks essentially the same apart the absence of the mentioned slight asymmetry.

The overall motion $w(x, t)$ depicted in Figs. 5-6 has been obtained as a linear combination of the flat plate vibration modes (see Eq. 7). The time-histories of the generalized coordinates $q_i(t)$ have been obtained from the integration of Eq. 8 with the Houbolt scheme. Thus, the explanation of the nonlinear behavior can be sought in the analysis of the generalized coordinates $q_i(t)$. For $\mu = 0.76$, the

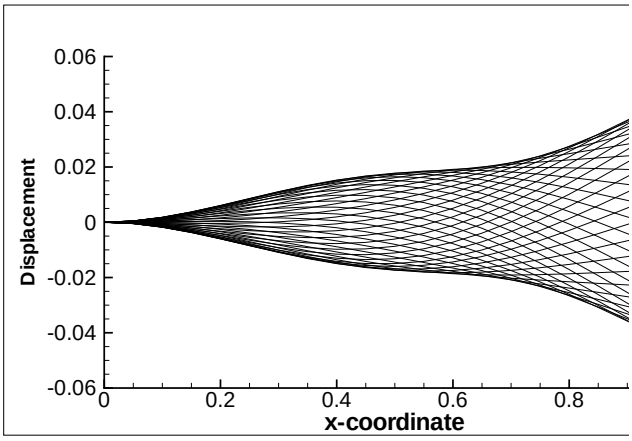

Figure 5: Snapshots of the flag motion for $h = 0.5$ and $U/U_{LF} = 1.01$ ($\mu = 0.76$ and $\alpha = 0.025$).

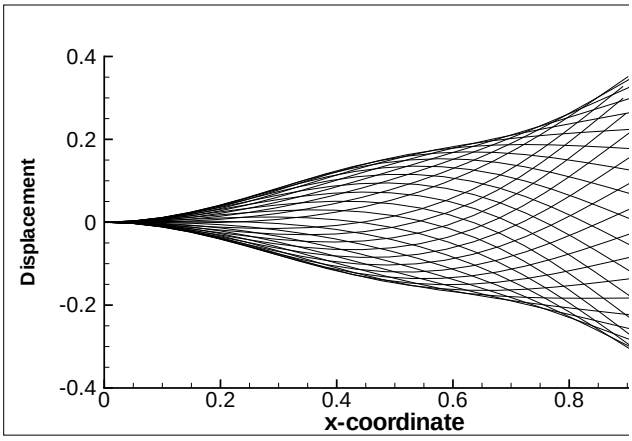

Figure 6: Snapshots of the flag motion for $h = 0.5$ and $U/U_{LF} = 1.33$ ($\mu = 0.76$ and $\alpha = 0.025$).

generalized coordinate that exhibits the largest periodic oscillations is q_1, as shown in Fig. 7 for the case $h = 0.5$. Also q_2 shows significant sinusoidal oscillations, whilst q_3 is subjected to comparatively small periodic oscillations. The periodic behavior of q_3 clearly shows superharmonics, which appear also in the infinite domain case but are less pronounced. Next, the bifurcation diagram in Fig. 8 for the generalized coordinates is built considering separately the positive and negative peaks for each simulation performed at different inflow velocities (in case of q_3, the highest peak in the period is considered). For all the velocity range, q_1 and q_2 provide significant oscillation amplitudes, whilst the remaining ones

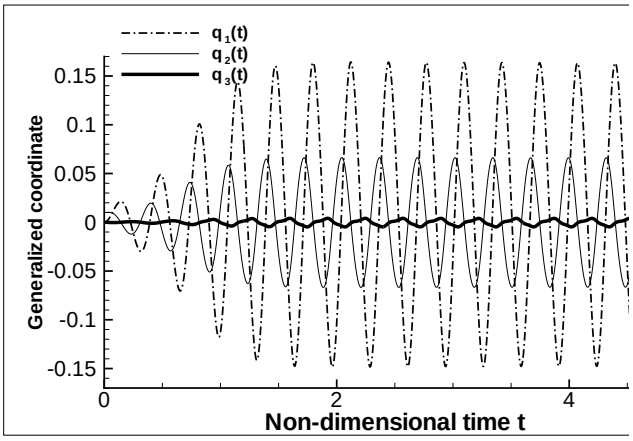

Figure 7: LCOs of the generalized coordinates q_1, q_2 and q_3 for $h = 0.5$ and $U/U_{LF} = 1.33$ ($\mu = 0.76$ and $\alpha = 0.025$).

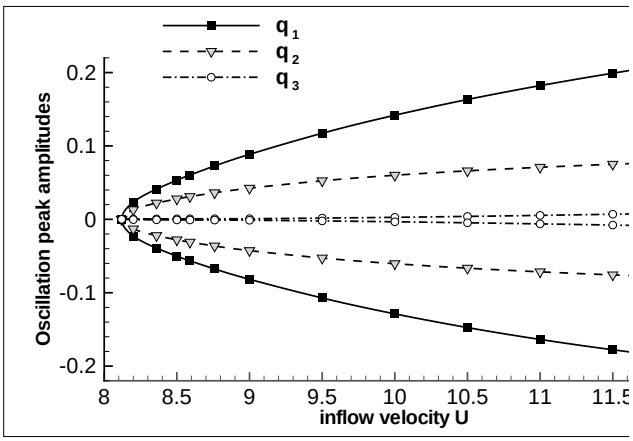

Figure 8: Bifurcation diagrams relative to the generalized coordinates q_1, q_2 and q_3 for $h = 0.5$ and $U/U_{LF} = 1.33$ ($\mu = 0.76$ and $\alpha = 0.025$).

scarcely contribute to the persistent flag motion. It is worth recalling that, since the coupled system is not available in analytical form like it occurs, for instance, for 2D aeroelastic theory of wing sections, no computation of critical (usually, complex conjugate) eigenvectors can be carried out.

Next, the dynamical analysis focuses on the trailing edge (TE) deflection of the plate as a representative point of the physical flag motion. The bifurcation diagram shown in Fig. 9 (upper branch = positive peaks, lower branch = negative peaks) indicates that a near-parabolic dependence of the TE oscillations on

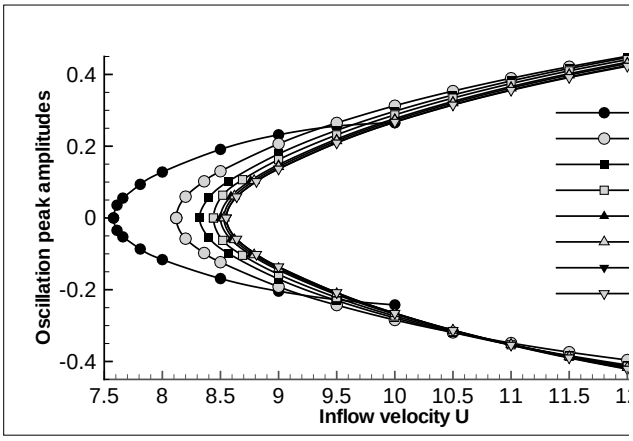

Figure 9: Bifurcation diagram for oscillations amplitude at the flag trailing edge ($\mu = 0.76$ and $\alpha = 0.025$).

h is present for almost all the considered ground clarences. However, a different feature is present here with respect to standard Hopf bifurcations. Oscillations amplitudes on the side far from the ground (positive peaks) are larger in absolute value than those achieved in oscillations toward the ground (negative peaks). This fact implies that Hopf bifurcation loses its symmetry with respect to the unstable fixed point solution (zero solution, the dynamical system is autonomous) as a consequence of the unsymmetrical behavior of the flag. The reason of this asymmetry lies not in the structural restoring force but in the different aerodynamic force generated during the upward and downward oscillation cycles.

Additional considerations about this asymmetry can be made if new variables are introduced. Next, let us define:

$$\hat{U} = (U - U_{LF})/U_{LF}, \tag{28}$$

$$\hat{W} = 1/2\left(W^{+} - W^{-}\right) \tag{29}$$

$$\overline{W} = 1/2\left(W^{+} + W^{-}\right), \tag{30}$$

where $\hat{U}$ is the normalized variation of the flow speed with respect to the flutter speed, $\hat{W}$ is the peak-to-peak semi-amplitude of LCOs and $\overline{W}$ is the offset (mean value) of oscillations with respect to zero. The analysis of the dependence of W, $\hat{W}$ and $\overline{W}$ with respect to $\hat{U}$ shows some interesting features. In Fig. 10 the positive part of the bifurcation diagrams relative to the different ground clearances in the original peak variable W collapse together for $h \geq 0.5$ (moderate ground effect). In extreme ground effect and in particular for $h = 0.25$ signifi-

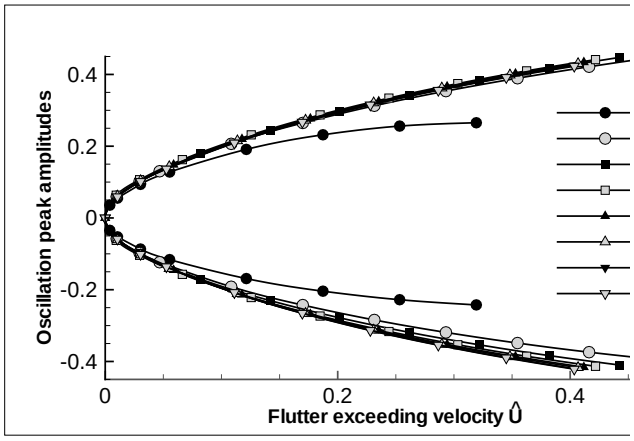

Figure 10: Positive peaks (upper curves) and negative peaks (lower curves) at the flag trailing edge with respect to the normalized flutter exceeding velocity ($\mu = 0.76$ and $\alpha = 0.025$).

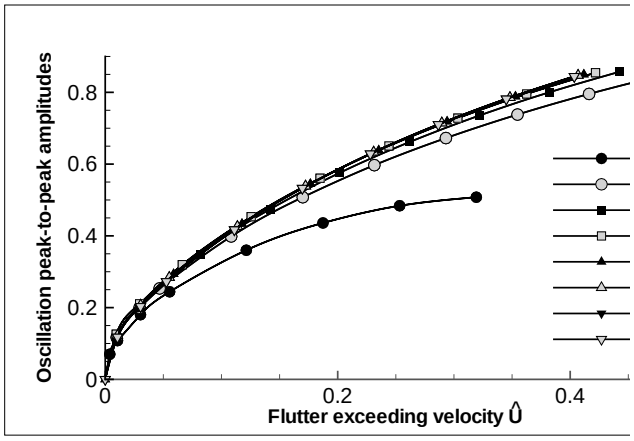

Figure 11: Bifurcation diagram for oscillations amplitude at the flag trailing edge ($\mu = 0.76$ and $\alpha = 0.025$).

cant differences appear. The bifurcation diagram (Fig. 11) in the new variable $\hat{W}$ confirms the uniqueness of extreme GE with respect to moderate GE, pointing out that an anticipation of the flutter regime is counterbalanced by an overall amplitude reduction of LCO in the postcritical regime. The offset of the peak average represented by $\overline{W}$ is represented in Fig. 12. The offset grows linearly with $\hat{U}$, except, again, for the extreme GE case $h = 0.25$.

Another feature to be carefully considered is the dependence of the frequency of LCO with respect the distance from the ground. In particular, in Fig. 13, the

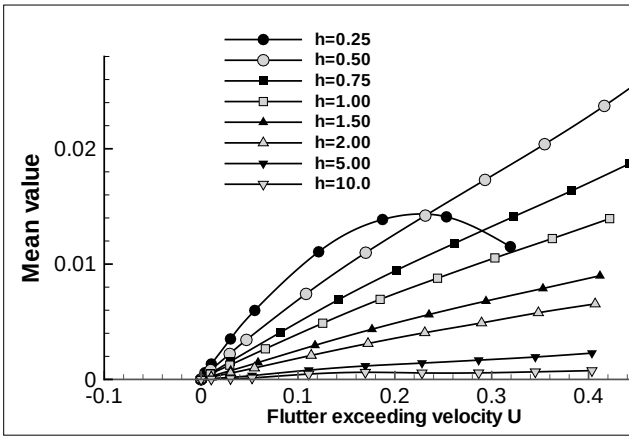

Figure 12: Bifurcation diagram for LCO offsets at the flag trailing edge ($\mu = 0.76$ and $\alpha = 0.025$).

so-called flutter frequency, *i.e.*, the LCO frequency at the critical speed, decreases toward an asymptotic value as long as ground clearance grows. This evidence was already highlighted also in the case of the aeroelastic typical section and is related to the faster response induced on the coupled flag dynamics by the presence of the ground. However, in the present case, variations are less evident (only 2% increment passing from $h = \infty$ to $h = 0.25$).

In Fig. 14 the LCO frequency for flags at different ground clearances is plotted versus the inflow velocity. The frequency increases with the inflow velocity and, for the same inflow velocity, the frequency increases if the flag is closer to the ground. These trends suggests a possible explanation for the significant reduction of LCO amplitudes at very low distances from the ground ($h = 0.25$). The power dissipated by the structure is proportional to $\dot{w}(x,t)^3$, the vertical flag velocity, which has a cubic dependence on ω. Thus, this dissipated power grows as long as h is decreased and this introduces a significant power take-off which stabilizes the system at lower values of the LCO amplitude. This effect is however evident only at $h = 0.25$, since a dependence of $\omega(U)$ on h similar to that shown in Fig. 13 occurs.

4.3. Experimental evidence of flutter onset in GE

As mentioned before, some tests were carried out for providing an experimental confirmation of the reduction of flutter speed in GE. This experimental campaign was intended just for highlighting a flutter speed reduction in GE with respect to the case without the 'ground' panel (vertical panel behind the flag, see

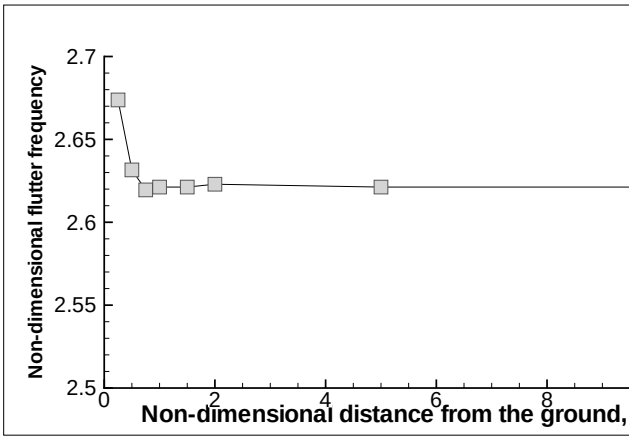

Figure 13: Frequency of LCO with respect to the ground clearance ($\mu = 0.76$ and $\alpha = 0.025$).

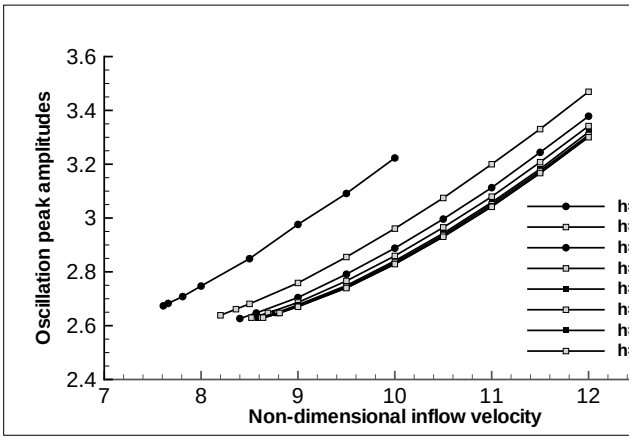

Figure 14: Frequency of LCO with respect to the inflow velocity ($\mu = 0.2$ and $\alpha = 0.025$).

Fig. 3). Because of several uncertainties in modelling or measuring some physical parameters (one for all, the effective inflow velocity) the experimental data cannot be used for validating the numerical simulation results. The overall motion is represented with several pictures shown in Figs. 15-17 and taken at equally spaced time instants with $\Delta t = 0.015625\, s$. The greyscale image has been inverted to enhance the flag contour. The distance from the ground panel was equal to $0.13\, m$ and the towing tank speed is $6.05\, m/s$. The depicted motion then concerns the ground effect in post-critical regime, since the nominal flutter speed, set equal to the speed of the carriage, is about $6.0\, m/s$ (see Table 1). In each figure, the

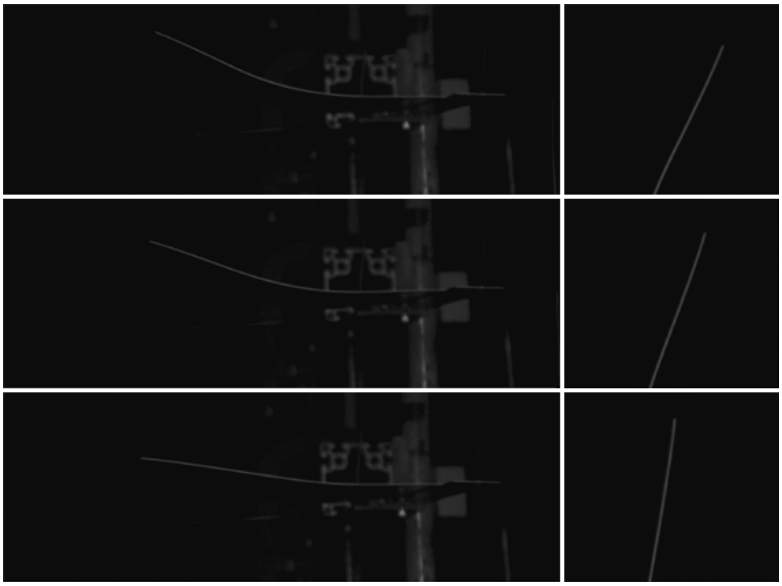

Figure 15: Snapshots of the flag motion for $h = \infty$ and $U/U_F = 1.325$ (negative image).

images relative to three different time instants have been put together. For each time instant, the side view of the entire flag is represented on the left part of the figure, whereas a detail of the flag tip, recorded with the second camera, is shown on the right part. The flag shows relevant periodic oscillations as expected, with a period lasting about $0.140\,s$ and clearly asymmetric with respect the rest plate position. The correspondent frequency of motion in GE is about the same value of the motion frequency relative to the unbounded domain case, that is experimentally estimate around $7.14\,Hz$. In fact, the uncertainty in the frequency estimation with the recorded motion sampling do not allow finding out small differences with and without GE.

The most relevant result of this experimental campaign is the reduction of about 4.7% in the nominal flutter speed, bringing the velocity from $6.3\,m/s$ to $6.0\,m/s$ when the ground panel is mounted. This percentage reduction, as well as the flutter frequency, is close to the value predicted with theory for the case $\mu = 0.76$. However, this is only an indication because other parameters in the simulation can not be considered to be truly representative of the tested flag.

4.4. Sensitivity of flag GE to plate parameters

The way by which certain features characterize the flag dynamics in GE are significantely affected by the mass ratio μ and the damping coefficient α. There-

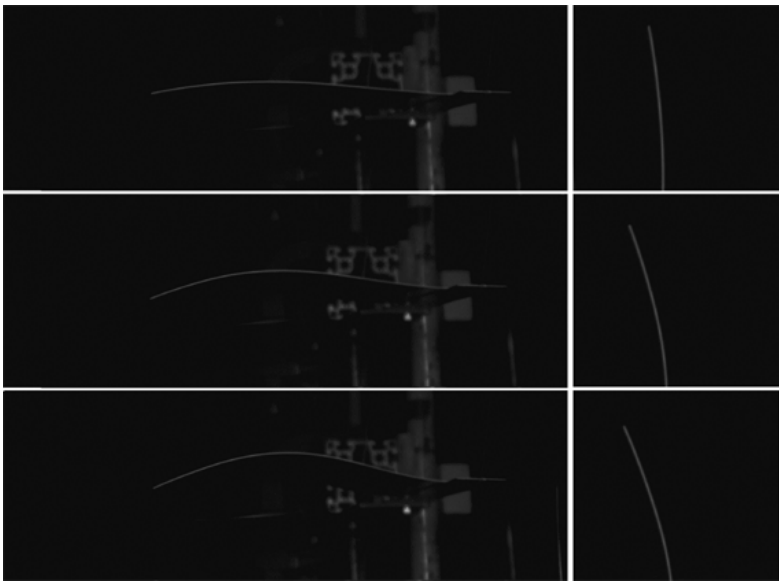

Figure 16: Snapshots of the flag motion for $h = \infty$ and $U/U_F = 1.325$ (negative image).

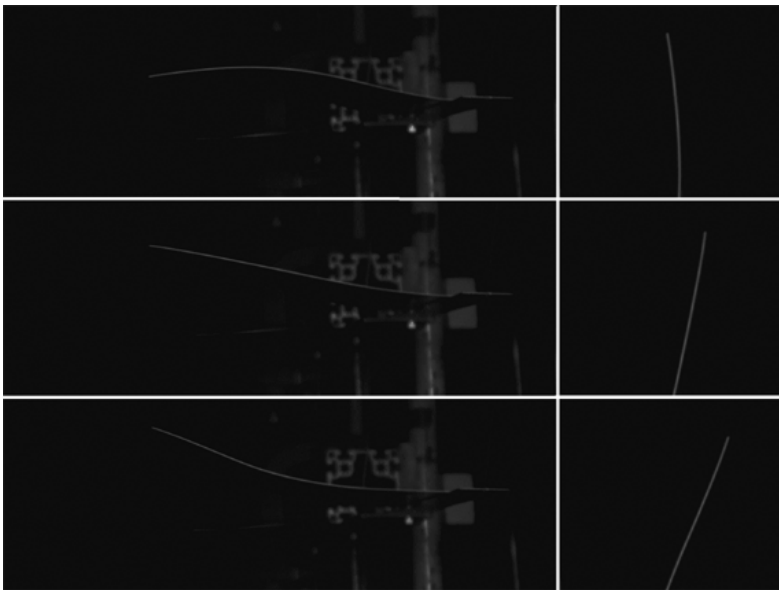

Figure 17: Snapshots of the flag motion for $h = \infty$ and $U/U_F = 1.325$ (negative image).

fore, it is instructive considering the case already treated by Tang and Paidoussis (2007) setting $\mu = 0.2$ and $\alpha = 0.004$. However, since in Tang and Paidoussis

Ground distance	Flutter speed
$0.13\,m$	$6.0\,m/s$
∞	$6.3\,m/s$

Table 1: Data relative to flutter onset.

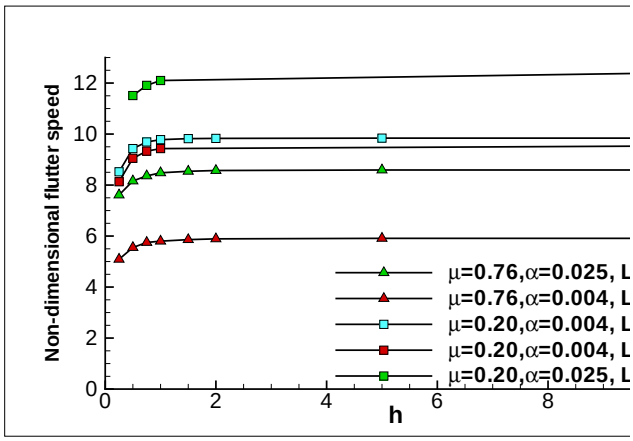

Figure 18: Sensitivity of the dependence of flutter speed U_{LF} on the ground clearance h for several plate parameters.

(2007) both μ and α are different (and even the inlet length l_0), some intermediate cases will be also considered to appreciate separately the sensitivity to each parameter.

The first comparison is relative to the sensitivity of flutter speed on the ground clearance (see Fig. 18). It is worth noting that both a decrease in μ (larger structural inertia force) and an increase in α (larger damping force) make the flutter velocity grow, *i.e.*, the system becomes more stable. Beside this main observation, it is worth noting that, as expected, there is also a slight effect of l_0 on the flutter velocity, which grows as the inlet length is reduced. The effect of these parameters on the frequency of flutter at the critical velocity follows the trend already highlighted before in Fig. 13: comparing two cases, if the flutter velocity reduces, the flutter frequency grows.

The snapshots of the flag motion in the case $\mu = 0.2$ and $\alpha = 0.001$ (Figs. 19 and 20) can be compared with the snapshots obtained with $\mu = 0.76$ and $\alpha = 0.025$ (Figs. 5-6). Reducing both μ and α leads to larger displacements and curvatures also in an unbounded domain (Figs. 19 and 20) and to an enhanced

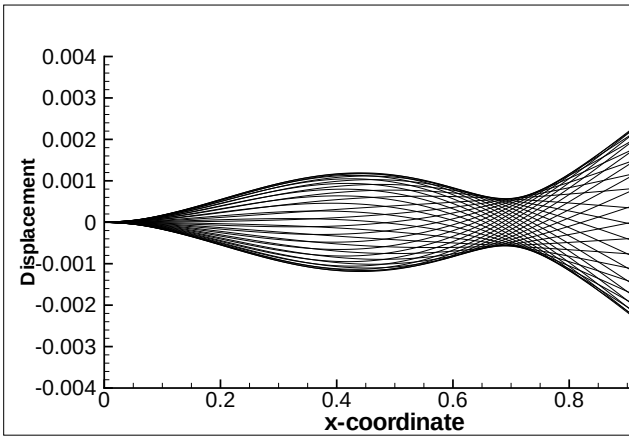

Figure 19: Snapshots of the flag motion for $h = \infty$ and $U/U_{LF} = 1.001$ ($\mu = 0.2$ and $\alpha = 0.004$).

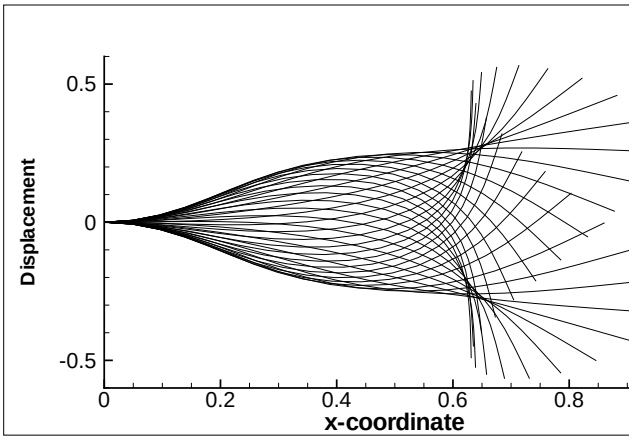

Figure 20: Snapshots of the flag motion for $h = \infty$ and $U/U_{LF} = 1.325$ ($\mu = 0.2$ and $\alpha = 0.004$).

asymmetry of motion (Figs. 21-22).

The explanation of the global behavior in terms of the overall displacement can be found again in the generalized coordinates $q_i(t)$. In Fig. 23 the time-history of the generalized coordinates $q_1(t)$, $q_2(t)$ and $q_3(t)$ are plotted for the case $h = 0.5$ and $U/U_{LF} = 1.33$. It is worth noting that the asymmetry of the flag motion is principally caused by the asymmetric oscillations of $q_1(t)$, whilst LCOs of $q_2(t)$ keep being symmetric. Also $q_3(t)$ is not symmetric but its contribution to the overall response is lower. It is also interesting noting that the presence of superharmonics has grown with respect to the case $\mu = 0.76$. This evidence is

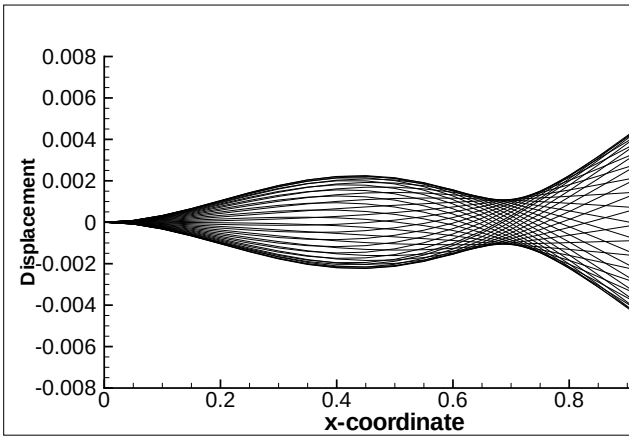

Figure 21: Snapshots of the flag motion for $h = 0.5$ and $U/U_{LF} = 1.002$ ($\mu = 0.2$ and $\alpha = 0.004$).

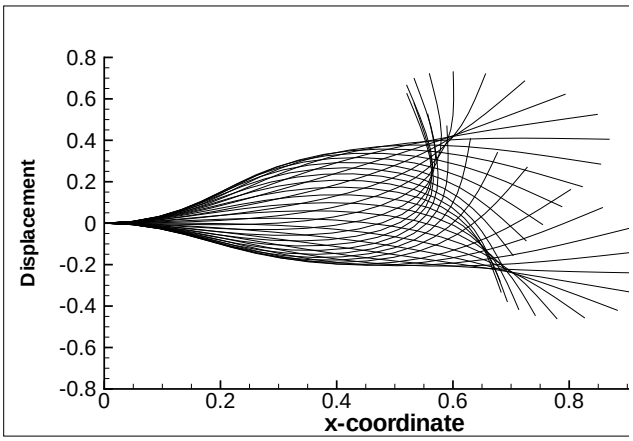

Figure 22: Snapshots of the flag motion for $h = 0.5$ and $U/U_{LF} = 1.333$ ($\mu = 0.2$ and $\alpha = 0.004$).

shown in the bifurcation diagram for the generalized coordinates q_i as well (see Fig. 24).

The bifurcation diagram relative to TE displacement for $\mu = 0.20$ is shown in Fig. 25. To better highlight the differences with respect to the other choice of the mass ratio, let us consider the comparison between the bifurcation diagrams in the plane $(\hat{U}, W)$ shown in Fig. 26 ($\mu = 0.2$) and in Fig. 10 ($\mu = 0.76$). In the case $\mu = 0.2$, the bifurcation diagrams at the different ground clearances differ both in the positive and in the negative branch, whereas for $\mu = 0.76$ the upper

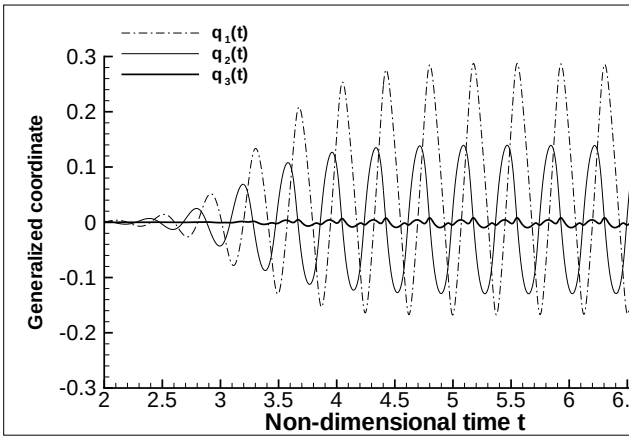

Figure 23: LCOs of the generalized coordinates q_1, q_2 and q_3 for $h = 0.5$ and $U/U_{LF} = 1.33$ ($\mu = 0.2$ and $\alpha = 0.004$).

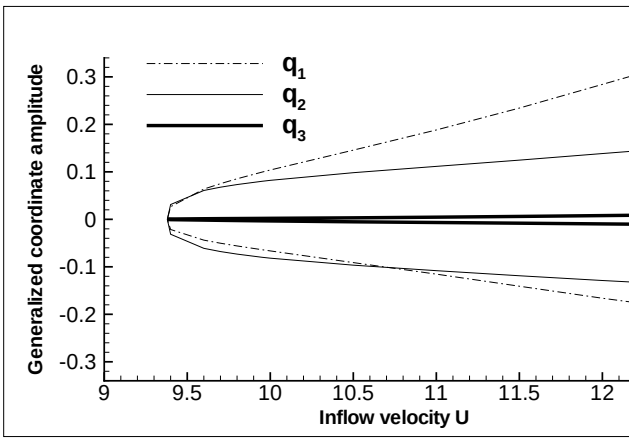

Figure 24: Bifurcation diagrams relative to the generalized coordinates q_1, q_2 and q_3 for $h = 0.5$ and $U/U_{LF} = 1.33$ ($\mu = 0.2$ and $\alpha = 0.004$).

branches merge together. The interpretation of this different behavior is enhanced if the bifurcation diagrams expressed in terms of $\hat{W}$ are taken into account. The curves of the amplitude of oscillation $\hat{W}$ in GE (Fig. 27) collapse into a single curve (note that it occurs also in extreme GE, *i.e.*, $h = 0.25$). The differences between the curves in Fig. 26 are due to the non-zero mean value of the LCOs, which changes with h.

This suggests that in this case the effectiveness of GE is in the anticipation of the flutter regime, while no variation of the bifurcation diagram is evident if the

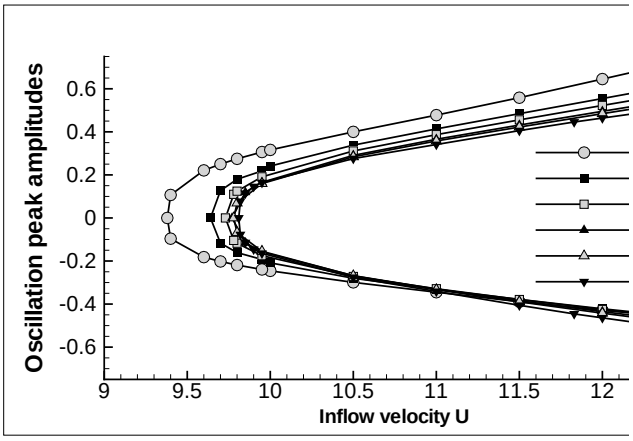

Figure 25: Bifurcation diagrams with respect to the inflow velocity U r elative to the flag TE displacement ($\mu = 0.2$ and $\alpha = 0.004$).

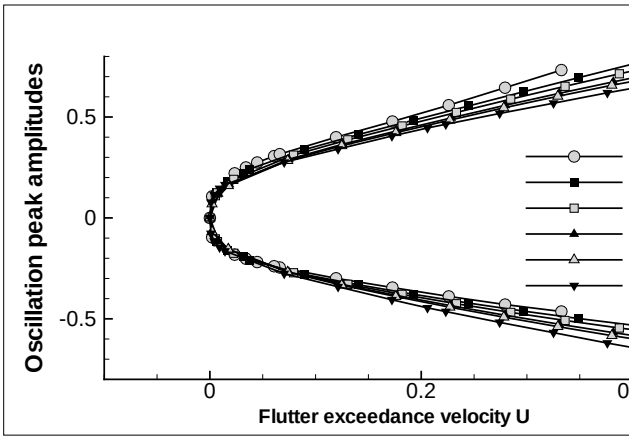

Figure 26: Bifurcation diagrams with respect to the normalized inflow velocity $\hat{U}$ of the flag TE displacement ($\mu = 0.2$ and $\alpha = 0.004$).

same $\hat{U}$ is considered.

5. Response analysis with POD

In this section the analysis of the fundamental modes that contribute to the numerical solution is carried out by using the proper orthogonal decomposition (POD). The POD is a multivariate statistical method that aims to obtain a compact representation of a dataset, regardless of the origin of the data. The POD

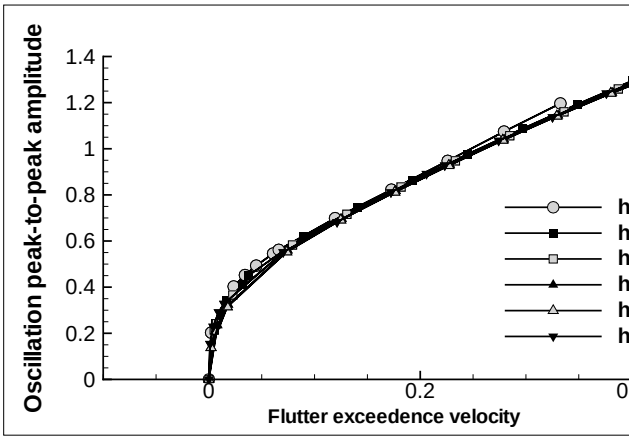

Figure 27: Bifurcation diagrams with respect to the normalized inflow velocity $\hat{U}$ of the flag peak-to-peak TE displacement ($\mu = 0.2$ and $\alpha = 0.004$).

extracts an orthonormal basis (proper orthogonal modes, POMs) to decompose the analyzed dataset, so that the projection of the data onto these basis functions contains as much energy as possible. The method, often called Karhunen-Loeve decomposition from the name of the authors that stated the method (Karhunen, (1946); Loeve, (1955)), has appeared in literature with various names depending on the area of application. The first applications of POD in the field of structural dynamics date back to the nineties and were mainly devoted to nonlinear problems. In these applications the technique aims to extract dominant structures from the system response data in order to model the spatial distribution of energy in the dynamics of the system and to construct low-dimensional models. For an extended review about the use of the POD for dynamical characterization and order reduction of mechanical systems, it is possible to refer to Kerschen et al. (2005). In the field of structural dynamics of linear systems, several papers treated the relationship between the POMs and the LNMs. Feeney and Kappagantu (1998) proved the convergence of the POMs to the LNMs for discrete systems in the case of undamped free vibration. Later, Feeny and his co-authors (2002)-(2003) extended the treatment to the case of continuous systems and to the case of randomly excited systems. Mariani and Dessi (2012) applied POD for identifying LNMs of a floating structure, demonstrating the possibility of using band-pass pre-filtering of experimental data when the mass distribution is unknown. In the present case, the homogeneous mass per length distribution (2D model) allows identifying the LNMs without the need of data filtering. The fundamental equa-

tion for applying POD is (see Mariani and Dessi (2012) for further details about the POD implementation):

$$\mathsf{R}\,\mathsf{p} = \sigma \mathsf{p}, \tag{31}$$

where R is the symmetric, definite positive covariance matrix, p is the eigenvectors of R also named as POM and σ is the eigenvalues or proper orthogonal value (POV). A particular feature in the present application is relative to data given as input to POD. The vertical and horizontal displacements considered for the analysis are relative to 21 points, equally spaced along the beam representing the 2D flag section with $\Delta s = 1/20$. Thus, the vector of processed time-histories is made of 42 components but, because of the algebraic relation between the u and w components (beam inextensibility), the independent components are 21. It is worth noting that the normalization of eigenvectors based on unity norm $\mathsf{p} \cdot \mathsf{p} = 1$ misses the constraint about the length of the flag that must be equal to unity, *i.e.*,

$$\int_{\xi_0}^{\xi_1} \sqrt{[x'(\xi)]^2 + [z'(\xi)]^2}\, d\xi = 1, \tag{32}$$

where ξ is a parameter running over the (ideally) continuous POM curve, $x(\xi)$ and $z(\xi)$ are the point coordinates and $'$ denotes in the above equation the derivative with respect to ξ. Therefore, scaling of p is done according to the above condition (expressed in discrete form) to meet this requirement. It is worth also remarking that the number of significant POD modes can not overcome the number of modes ($M = 5$) used in the modal decomposition.

The analysis based on POD says that the change in the shape of modes is less important than the variation of energy associated to POD modes. In the following Figs. 28-29 the POMs relative to different mass ratios, *i.e.*, $\mu = 0.76$ and $\mu = 0.2$, are shown. In both cases, the flow velocity is relative to the post-critical regime, where relatively large LCO have already appeared. The depicted POMs are subjected to the condition that the percentage associated energy, defined as:

$$\hat{\sigma}_i = \sigma_i / \sum_{i=1}^{N_{dof}} \sigma_i, \tag{33}$$

and ranging from 0 to 1, is greater than 0.001. There is not much difference between the considered mass ratios if the POM shape is taken into account. These differences are even smaller if POMs relative to different velocities (near-critical and post-critical regimes) are compared to each other. It is much more interesting

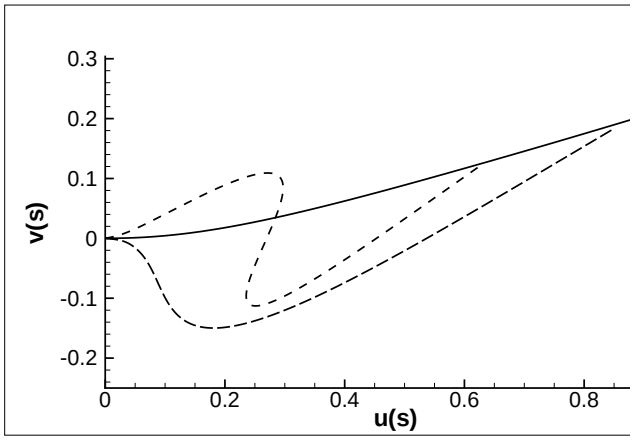

Figure 28: POM shapes for $\mu = 0.76$, $\alpha = 0.025$, $U = 1.29$ and $h = 0.5$.

comparing the contribution of each POM to the overall response (LCOs) in the considered cases by looking at the percentage energy $\hat{\sigma}$ in Table 5.

A general consideration is about the evidence that only the first and the second mode (or POM) contribute significantly to the overall flag response. The third mode gives a very small contribution and the fourth mode practically do not participate to the solution. With $\mu = 0.76$, the first mode relevance grows with respect to the second one as the velocity is increased. This is true both in infinite domain and in GE, with values substantially close to each other. A different trend seems present with $\mu = 0.2$, when the percentage of the first mode contribution initially decreases and grows again with the inflow velocity. Though not comparable with the first two modes, the third POM is slightly more significant in the case $\mu = 0.20$.

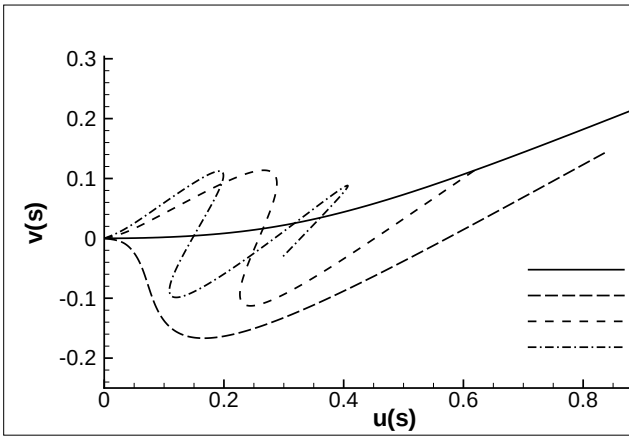

Figure 29: POM shapes for $\mu = 0.20$, $\alpha = 0.004$, $U = 1.367$ and $h = 0.5$.

6. Conclusions

The aeroelastic behavior of a flexible plate subjected to a uniform inflow is investigated in ground effect. The 2D model developed by Tang and Paidoussis (2007), coupling a potential unsteady flow solver (Lumped Vortex Panel Method) with modal equations of a nonlinear Euler-Bernouilli beam, has been extended to account for the presence of a rigid plane at a finite distance from the flag. The numerical results and the preliminary experimental tests show that the system experiences flutter in ground effect at an inflow velocity lower than that observed in an unbounded flow domain. Sensitivity of critical velocity and asymmetry of limit-cycle oscillations to several plate parameters (mass ratio, damping coefficient, inlet length) has been analyzed using also proper orthogonal decomposition.

The assessed reduction of the flutter velocity confirms similar results obtained for the case of 2D aeroelastic sections (see Nuhait and Mook (2010) and Dessi et al. (2012)). Indeed, the 2D hypothesis underestimates the flutter velocity, as pointed out by Eloy et al. (2012) in absence of GE. However, it is still unclear whether or not the 2D assumption emphasizes the flutter velocity reduction in GE. Nonetheless, the experimental tests has demonstrated that a similar trend exists also for the 3D problem. This feature is beneficial in the perspective of using the flag as an energy harvesting device because a less demanding wind velocity for the flutter onset is required. Apparently, if one considers uniquely the flag TE, no significant changes are present in the shape of the bifurcation curve relating the amplitude of limit-cycle oscillations to the flow velocity. However, depending on the system exploited for converting mechanical energy into electrical one,

μ	h	U	1st POV%	2nd POV%	3rd POV%	4th POV
0.76	∞	1.01	79.762	20.237	0.000	0.000
0.76	∞	1.17	83.110	16.889	0.001	0.000
0.76	∞	1.29	85.094	14.905	0.002	0.000
0.76	0.5	1.01	78.355	21.645	0.000	0.000
0.76	0.5	1.17	81.723	18.275	0.001	0.000
0.76	0.5	1.01	83.882	16.115	0.002	0.000
0.20	10.0	1.001	89.270	10.730	0.000	0.000
0.20	10.0	1.17	73.133	26.851	0.015	0.001
0.20	10.0	1.17	73.324	26.652	0.023	0.002
0.20	0.5	1.002	89.605	10.395	0.000	0.000
0.20	0.5	1.17	71.436	28.542	0.021	0.001
0.20	0.5	1.367	72.102	27.861	0.035	0.002

Table 2: Percentage energy $\hat{\sigma}$ associated to POMs.

e.g., piezoelectric patches, the flag curvatures may be of major concern. A relevant effect on the final results is due to the physical parameters of the flag, as highlighted already by different authors: in 2D, the mass ratio of the flag along with the material damping have a consequence on the design of the flag and, in GE, may enhance or not asymmetry in the LCOs. Thus, as pointed out before, the case $\mu = 0.2$ shows curvatures much more relevant than the case $\mu = 0.76$ and differences also appear, for the same mass ratio, between $h = 0.5$ and $h = \infty$.

The POD analysis allows estimating the energy fraction associated to each mode. Energy fractions show that the energy distribution is fundamentally limited to the first and second mode and depend slightly on GE and other flag parameters.

The results obtained in this paper in absence of GE are in close agreement, as expected, with those obtained by Tang and Paidoussis (2007). Indeed, some choices in the numerical model, *e.g.*, the wake length, may slightly affect the final results, but the numerical model seems sufficiently robust after performing a convergence analysis. It is worth remarking that no experimental validation of the effectiveness of the numerical model (*i.e.*, assumptions plus solvers) in predicting the flutter velocity has been proposed yet. In this preliminary experimental campaign devoted to the confirmation of the flutter speed reduction, the focus has been on preparing an experimental set-up that could be hosted on the towing-tank carriage with minimum aerodynamic interference with the carriage structure. Identification of the flag parameters with special emphasis on the Young modulus

and damping as well as monitoring of the inflow conditions is next step toward experimental validation of the simulation results.

Alben, S., Shelley, M. J., 2008. Flapping states of a flag in an inviscid fluid: bistability and the transition to chaos. Phys. Rev. Lett. 100, 074301 1-4.

Belanger, F., Paidoussis, M. P., De Langre, E., 1995. Time-Marching Analysis of Fluid-Coupled Systems with Large Added Mass, AIAA Journal 33 (4), 752-757.

De Langre, E., 2012. Methodological advances in predicting flow-induced dynamics of plants using mechanical-engineering theory. Journal of Experimental Biology 215, 914-921.

Dessi, D., Mastroddi, F. (2008). Limit-cycle stability reversal via singular perturbation and wing-flap flutter. Journal of Fluids and Structures 19(6), 765-783.

Dessi, D., Mastroddi, F. Mancini, S., 2013. Analytical formulation of 2-D aeroelastic model in weak ground effect. Journal of Fluids and Structures 42, 270-295.

Doar, O., Michelin, S., 2011. Piezoelectric coupling in energy-harvesting fluttering flexible plates: linear stability analysis and conversion efficiency. Journal of Fluids and Structures 27(8), 1357-1375.

Doar, O., Sauzade, M., Eloy, C., 2011. Flutter of an elastic plate in a channel flow: confinement and finite-size effects. Journal of Fluids and Structures 27, 7688.

Dowell, E. H., 1966. Nonlinear oscillations of a fluttering plate. AIAA Journal 4(7), 1267-1275.

Eloy, C., Kofman, N., Schouveiler, L., 2012. The origin of hysteresis in the fag instability. Journal of Fluid Mechanics, 691, 583-593.

Feeny, B. F., Kappagantu, R., 1998. On the physical interpretation of proper orthogonal modes in vibrations. Journal of Sound and Vibration 211(4), 607-616.

Feeny, B. F., 2002. On the proper orthogonal modes and normal modes of continuous vibration systems. Journal of Vibration and Acoustics, 124(1), 157-160.

Feeny, B. F., Liang, Y., 2003. Interpreting proper orthogonal modes in randomly excited vibration systems. Journal of Sound and Vibration, 265(5), 953-966.

Huang, L., 1995. Flutter of cantilevered plates in axial flow. Journal of Fluids and Structures 9, 127-147.

Karhunen, K., 1946. Under lineare methoden in der wahrscheinlichkeitsrechnung. Annals of Academic Science Fennicae Series, A 1, Math. Phys., 37(2).

Katz, J., Plotkin, A., 2001. Low speed aerodynamics (2^{nd} Ed.). Cambridge University Press, NY.

Kerschen, G., Golinval, J. C., Vakakis, A. F., Bergman, L. A., 2005. The method of proper orthogonal decomposition for dynamical characterization and order reduction of mechanical systems: an overview. Nonlinear Dynamics 41, 147-169.

Loeve, M. M., 1955. Probability theory, Von Nostrand, Princeton, New Jersey.

Mariani, R. and Dessi, D., 2012. Analysis of the global bending modes of a floating structure using the proper orthogonal decomposition. Journal of fluids and structures 28, 115-134.

Nuhait, A. O., Mook, D. T., 2010. Aeroelastic Behavior of Flat Plates Moving Near the Ground. Journal of Aircraft 47(2), 464-474.

Semler, C., Li, G. X., Padoussis, M. P., 1994. The non-linear equations of motion of pipes conveying fluid. Journal of sound and vibration 169(5), 577-599.

Tang, L., Paidoussis, M.P., 2007. On the instability and the post-critical behavior of two-dimensional cantilevered flexible plates in axial flow. Journal of Sound and Vibration 305, 97-115.

Tang, L., Padouissis, M.P., Jiang, J., 2009. Cantilevered flexible plates in axial flow: Energy transfer and the concept of flutter-mill. Journal of Sound and Vibration 326, 263-276.

Theodorsen, T., 1935. General theory of aerodynamic instability and mechanism of flutter. NACA Technical Report 496.

Watanabe, Y., Suzuki, S., Sugihara, M., Sueoka, Y., 2002. An experimental study of paper flutter. Journal of Fluids and Structures 16(4) 529-542.

Watanabe, Y., Isogai, K., Suzuki, S., Sugihara, M., Sueoka, Y., 2002. A theoretical study of paper flutter. Journal of Fluids and Structures 16(4) 543-560.

List of Figures

List of Tables